The Astrophysical Journal Letters, 949:L10 (9pp), 2023 May 20 https://doi.org/10.3847/2041-8213/acd33e

Polarized X-Rays from Windy Accretion in Cygnus X-1

Juri Poutanen[1], Alexandra Veledina[1,2], and Andrei M. Beloborodov[3,4]
[1] Department of Physics and Astronomy, FI-20014 University of Turku, Finland; juri.poutanen@utu.fi
[2] Nordita, KTH Royal Institute of Technology and Stockholm University, Hannes Alfvéns väg 12, SE-106 91 Stockholm, Sweden
[3] Physics Department and Columbia Astrophysics Laboratory, Columbia University, 538 West 120th Street, New York, NY 10027, USA
[4] Max Planck Institute for Astrophysics, Karl-Schwarzschild-Str. 1, D-85741 Garching, Germany
Received 2023 February 22; revised 2023 May 3; accepted 2023 May 5; published 2023 May 22

Abstract

Recent X-ray polarimetric data on the prototypical black hole X-ray binary Cyg X-1 from the Imaging X-ray Polarimetry Explorer present tight constraints on accretion geometry in the hard spectral state. Contrary to general expectations of a low, $\lesssim$1% polarization degree (PD), the observed average PD was found to be a factor of 4 higher. Aligned with the jet position angle on the sky, the observed polarization favors geometry of the X-ray emission region stretched normally to the jet in the accretion disk plane. The high PD is, however, difficult to reconcile with the low orbital inclination of the binary $i \approx 30^\circ$. We suggest that this puzzle can be explained if the emitting plasma is outflowing with a mildly relativistic velocity $\gtrsim 0.4\,c$. Our radiative transfer simulations show that Comptonization in the outflowing medium elongated in the plane of the disk and radiates X-rays with the degree and direction of polarization consistent with observations at $i \approx 30^\circ$.

Unified Astronomy Thesaurus concepts: Stellar mass black holes (1611); Starlight polarization (1571); Accretion (14); Polarimetry (1278); X-ray binary stars (1811)

1. Introduction

Accreting black holes (BHs) in X-ray binaries display different spectral states, "hard" and "soft," distinguished by the spectral shape and the variability properties (Zdziarski & Gierliński 2004; Remillard & McClintock 2006). In the soft state, the dominant contribution to the X-ray flux comes from a thermal-looking spectrum peaking at ~1 keV energies, which is commonly attributed to the multi-temperature blackbody accretion disk (Novikov & Thorne 1973; Shakura & Sunyaev 1973). An additional power-law-like tail is likely produced by inverse Compton scattering by relativistic electrons in the corona (Poutanen & Coppi 1998; Gierliński et al. 1999; Zdziarski et al. 2001; McConnell et al. 2002). In the hard state, the spectrum is power-law-like in the standard X-ray band and shows a cutoff at ~100 keV, which is interpreted as a signature of thermal Comptonization in a hot electron medium. The geometry of this medium and the source of soft seed photons is a matter of debate (Done et al. 2007; Poutanen & Veledina 2014; Bambi et al. 2021).

The most popular model for the hot medium is the inner hot, geometrically thick, optically thin flow (e.g., Shapiro et al. 1976; Ichimaru 1977; Poutanen et al. 1997; Esin et al. 1998; Yuan & Narayan 2014). It is supported by a number of arguments, including correlations between characteristic variability frequencies of the aperiodic noise (Axelsson et al. 2005), the central frequencies of quasiperiodic oscillations (Pottschmidt et al. 2003; Ibragimov et al. 2005), the spectral slope of Comptonization continuum, and the amplitude of Compton reflection (Zdziarski et al. 1999, 2003).

A corona on top of a cold disk near the BH was also considered a source of hard X-rays (Haardt & Maraschi 1993). Simple models with a slablike corona were found to produce too-soft X-ray spectra (Stern et al. 1995) because a large fraction of the coronal emission becomes reprocessed to soft radiation by the underlying disk, and the reflection component becomes stronger than the observed one. It was suggested that reprocessing could be reduced by the high ionization of the disk surface (Nayakshin & Dove 2001; Malzac et al. 2005; Poutanen et al. 2018).

The observed spectrum may also be explained by a mildly relativistic outflowing corona, which beams hard X-rays away from the accretion disk, reducing their reflection and reprocessing (Beloborodov 1999; Malzac et al. 2001). Outflows are generally expected to accompany the heating process in the magnetized corona. For instance, magnetic flares eject plasma, resembling solar flares. Furthermore, if energy is released in compact flares, the plasma can become dominated by electron–positron pairs (Svensson 1984; Stern et al. 1995; Poutanen & Svensson 1996), which have a tiny inertial mass. In this case, the plasma flows out with a saturated speed controlled by the local radiation field. Coronal outflows have also been observed in global simulations of accretion, which have begun to implement radiative effects in electron-ion plasma (Liska et al. 2022). Mildly relativistic "winds" are expected to surround the more relativistic "jets" seen in radio observations during the hard state (Fender 2001; Stirling et al. 2001).

In spite of a large body of data on timing, spectra, and imaging of BH X-ray binaries, there is still a large uncertainty in the geometry of their X-ray emission region. Polarization has long been anticipated to provide an opportunity to determine the accretion geometry (Lightman & Shapiro 1976). One of the best-studied BH X-ray binaries Cyg X-1 was observed with the Imaging X-ray Polarimeter Explorer (IXPE; Weisskopf et al. 2022) on 2022 May 15–21 and June 18–20. A rather high polarization degree (PD) = 4.0% ± 0.2% in the 2–8 keV range at the polarization angle PA = −20° ± 2°, consistent with the jet position angle (Stirling et al. 2001), was detected (Krawczynski et al. 2022). Various models for the X-ray emitting region, such as a slab corona, a static inner hot flow,

and conical or spherical lamppost corona at the disk rotation axis above the BH have been considered. Krawczynski et al. (2022) suggest that the data can be reproduced only by models where the emission region is extended orthogonally to the jet (which is itself presumably perpendicular to the accretion disk). However, none of the considered models reproduces the high PD at the measured inclination of $i = 27.5^{+0.8}_{-0.6}{}^{\circ}$ (Miller-Jones et al. 2021); higher inclination, $i \gtrsim 45^{\circ}$, was required in order to reproduce the data.

In this paper, we show that the observed PD can be reproduced if the hot medium forms an outflow from the accretion disk. The mildly relativistic speed of the outflow affects polarization of scattered radiation because the angular distribution of seed photons is significantly aberrated in the plasma rest frame (Beloborodov 1998). This results in a higher polarization of outgoing radiation at low inclinations. In Section 2 we describe the setup of the model, and Section 3 presents the results of our radiative transfer simulations. We discuss the obtained results and conclude in Section 4. Appendices A and B present the radiative transfer equation (RTE) describing our model and a few examples of simulations.

2. Models for Polarization

2.1. Geometry

We assume that the observed X-rays in the hard state of Cyg X-1 are produced close to the compact object within the hot medium. We consider three alternative geometries sketched in Figure 1:

(A) Hot corona covering the cold accretion disk (aka slab corona) with the seed unpolarized blackbody photons of temperature $kT_{\rm bb} = 0.1$ keV from the underlying accretion disk. Radiation produced by multiple Compton scattering in such a slab is polarized at a level of ∼10% (e.g., Poutanen & Svensson 1996; Schnittman & Krolik 2010).

(B) Hot medium situated within the truncated cold accretion disk; this model is usually referred to as a hot-flow model. Here the seed photons could be produced within the flow, for example, by the synchrotron emission of nonthermal electrons with the peak at around 1 eV (Malzac & Belmont 2009; Poutanen & Vurm 2009; Veledina et al. 2013) or by cold clouds embedded in the hot flow (Celotti et al. 1992; Poutanen et al. 2018; Liska et al. 2022). We consider the first case here.

(C) Same as model (B) but with the seed unpolarized photons coming from the outer cold truncated disk of the temperature $kT_{\rm bb} = 0.1$ keV. In this model, the incident angles of the seed photons are limited by the aspect ratio of the flow $h = H/R$ (see Appendix A for details).

For all models, the scattering geometry is approximated by a plane-parallel slab extended along the disk plane.

2.2. Parameters of the Outflow

The hot medium itself can be in a dynamical state, where in addition to the azimuthal and radial motions, some fraction of the accreting matter leaves the system in a mildly relativistic wind. For our simulations, to account for the influence of the wind on polarization properties, we assume that the whole hot medium has the vertical velocity (aka outflowing corona)

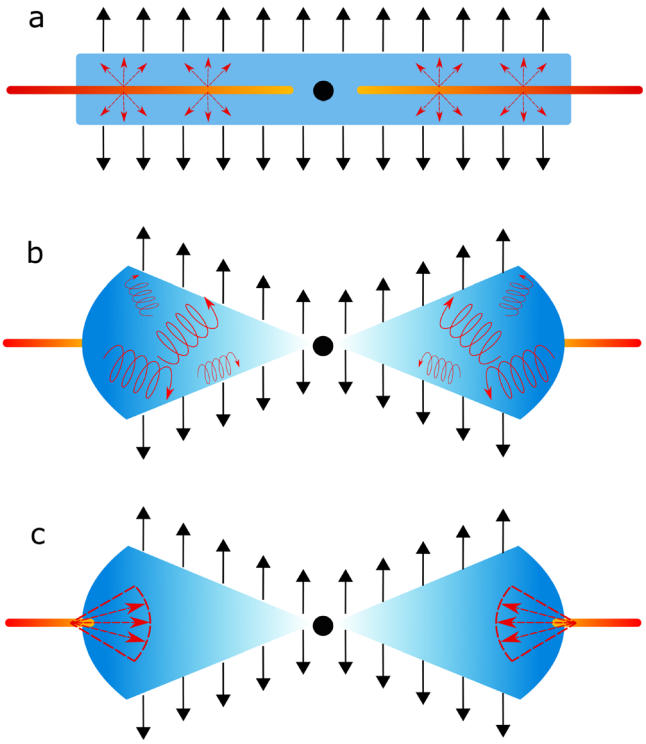

Figure 1. Three alternative geometries considered in the work: panel (a) the outflowing corona with the underlying cold disk producing seed photons corresponding to model (A), panel (b) is for the outflowing hot flow with the internal synchrotron seed photons corresponding to model (B), and panel (c) is for the outflowing hot flow with the seed photons from the outer truncated disk (model C).

following the profile

$$\beta(\tau) = \beta_0 \frac{\tau}{\tau_0}, \tag{1}$$

where τ is the Thomson optical depth measured from the central plane and τ_0 is the total optical depth through the corona. The flow diverges sideways at some height H, which leads to a rapid drop of density. This height then can be considered as the upper boundary of the outflow.

We note here that the continuity equation implies that $n_{\rm e}(z)\beta(z) = n_0\beta_0$ is uniform with z in a steady outflow. For the velocity profile given by Equation (1), the optical depth then can be expressed as

$$d\tau(z) = n_{\rm e}(z)\sigma_{\rm T}dz = \sigma_{\rm T}n_0\frac{\beta_0}{\beta(z)}dz = \sigma_{\rm T}n_0\frac{\tau_0}{\tau(z)}dz, \tag{2}$$

resulting in

$$\tau(z) = \tau_0\,(z/H)^{1/2}, \qquad \tau_0 = 2\sigma_{\rm T}n_0H. \tag{3}$$

We thus get the electron density and velocity dependence on height

$$n_{\rm e}(z) = n_0(z/H)^{-1/2}, \qquad \beta(z) = \beta_0(z/H)^{1/2}. \tag{4}$$

The densest part of the outflow near the mid-plane has a small optical depth $\tau(z) \propto \sqrt{z}$ and makes a negligible contribution to scattering, so the details of how the inflow becomes the outflow near the mid-plane are not very important.

Our model implies mass-loss rate from the disk of radius R of

$$\dot{M}_{\rm out} = 2\pi R^2 c\beta_0 n_0 m_{\rm p}\mu_{\rm e}, \quad (5)$$

where $\mu_{\rm e}$ is the mean molecular weight per electron in the outflow. On the other hand, the standard estimate for accretion rate in a disk with luminosity L and radiative efficiency ϵ is

$$\dot{M}_{\rm acc} = \frac{L}{\epsilon c^2} = \frac{\ell}{\epsilon}\frac{4\pi R_{\rm g} m_{\rm p} c}{\sigma_{\rm T}}, \quad (6)$$

where $\ell = L/L_{\rm Edd}$, $L_{\rm Edd} = 4\pi GMm_{\rm p}c/\sigma_{\rm T}$ is the Eddington luminosity and $R_{\rm g} = GM/c^2$ is the gravitational radius. This gives

$$\frac{\dot{M}_{\rm out}}{\dot{M}_{\rm acc}} = \frac{\epsilon R^2\mu_{\rm e}}{\ell}\frac{\sigma_{\rm T}\beta_0 n_0}{2R_{\rm g}} = \frac{\epsilon\mu_{\rm e}\beta_0\tau_0}{4\ell h}\frac{R}{R_{\rm g}}. \quad (7)$$

Our fiducial model has $h = 1$, $\beta_0 = 1/2$, and $\tau_0 = 1$. The observed luminosity of Cyg X-1 implies $\ell \sim 0.02$, assuming the BH mass $M \sim 10M_\odot$. Then, for an outflow made of electron-proton plasma ($\mu_{\rm e} = 1$), we find $\dot{M}_{\rm out}/\dot{M}_{\rm acc} \sim 6\epsilon R/R_{\rm g}$. This estimate is consistent with a large fraction of the accretion flow being diverted into an outflow before reaching the BH. A significantly lower estimate for $\dot{M}_{\rm out}$ is found if the coronal heating occurs intermittently in space and time, in magnetic flares. In this case, the local radiation density can reach values sufficient for copious $e^\pm$ pair production, reducing $\mu_{\rm e}$ and $\dot{M}_{\rm out}$.

2.3. Method

The parameters of the corona are the electron temperature $T_{\rm e}$, the Thomson optical depth τ_0, and the terminal velocity β_0, which is varied from 0 to 0.6. In the simulations, we considered $kT_{\rm e} = 100$ keV, which is close to the observed values (Gierlinski et al. 1997). To reproduce the spectral energy distribution of Cyg X-1 in the hard state (Gierlinski et al. 1997; Krawczynski et al. 2022), we iterated τ_0 to achieve the observed photon index $\Gamma = 1.6$ in the 2–10 keV energy range.

The RTE that accounts for multiple Compton scattering of linearly polarized radiation in the moving medium is given in Appendix A. The only difference with the previously considered static models is that the effect of relativistic aberration has to be taken into account. We start simulations with some initial τ_0 and solve the RTE in the plane-parallel (slab) approximation assuming azimuthal symmetry. Once the outgoing spectrum is obtained, we find the photon index Γ in the 2–10 keV range (for an observer at $i = 30°$) and correct τ_0. Iterations continue until the desired Γ is reproduced. The escaping polarized radiation is described by two Stokes parameters I and Q, with U being identically zero because of azimuthal symmetry. We can then define PD $= Q/I$, which is positive when the dominant direction of oscillations of the electric vector (aka the polarization vector) is parallel to the slab normal. If the polarization vector is perpendicular to the flow normal, then the PD is negative. For example, the optically thick electron-scattering atmosphere produces negative PD (Chandrasekhar 1960).

The basic physics that controls the polarization production can be described as follows. Polarization of radiation scattered in the hot flow once depends strongly on the angular distribution of the incoming seed photons. If they come from the underlying cold disk (and therefore beamed along the flow normal), the scattered radiation is polarized perpendicular to the flow normal (i.e., along the disk), resulting in negative PD. On the other hand, if they come from the outer truncated disk (i.e., sideways), the scattered radiation is polarized parallel to the normal, resulting in positive PD. In the latter case, polarization can reach 33% in an ideal case when photons are injected in a plane and scattering is coherent (Sunyaev & Titarchuk 1985; Poutanen et al. 2022). If the corona is moving upwards, external radiation will be affected by relativistic aberration, resulting in parallel polarization for $0.1 \lesssim \beta \lesssim 0.8$ (Beloborodov 1998). When photons undergo many scatterings in an optically thin plane-parallel medium, polarization is in general parallel to the flow normal independently of the angular distribution of seed photons.

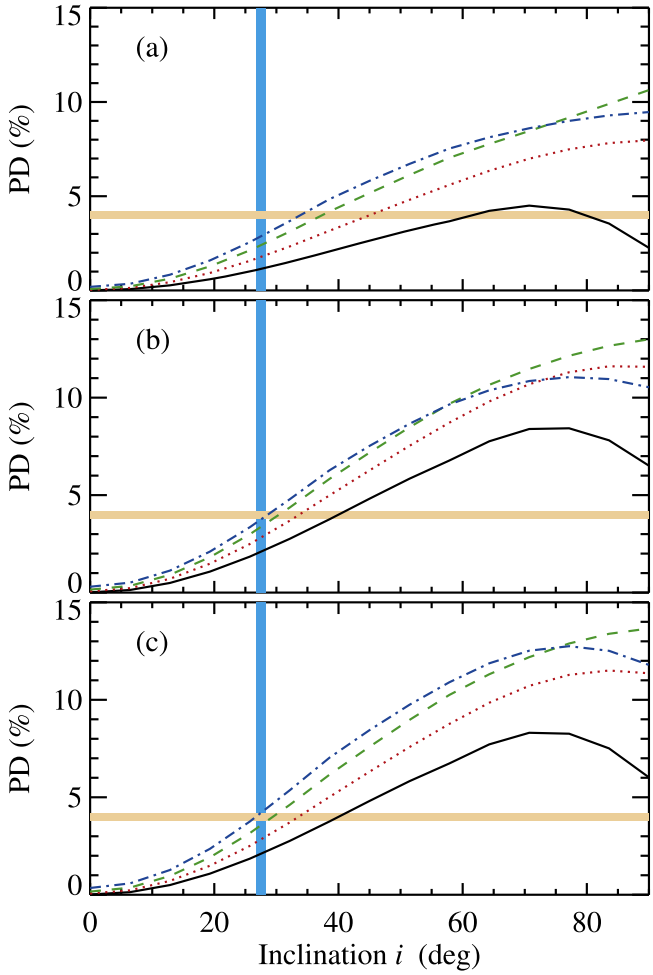

Figure 2. Angular distribution of the PD for different outflow velocities $\beta_0 = 0$ (black solid), 0.2 (red dotted), 0.4 (green dashed), and 0.6 (blue dotted–dashed) in the middle of the IXPE range at 4 keV for the three models are shown in Figure 1. Coronal parameters are $kT_{\rm e} = 100$ keV, $kT_{\rm bb} = 0.1$ keV, and $\Gamma = 1.6$. The vertical blue stripe marks the $i = 27.5^{+0.8}_{-0.6}°$ inclination (Miller-Jones et al. 2021) and the horizontal beige stripe corresponds to the observed X-ray PD from Cyg X-1 of 4.0% ± 0.2% (Krawczynski et al. 2022).

3. Results

Figure 2(a) shows the angular distribution of the PD for model (A) in the middle of the IXPE range at 4 keV. We see that for static corona, the peak in the PD is reached at ∼70°, while for the outflowing corona, the PD is growing with inclination more or less monotonically. This figure clearly

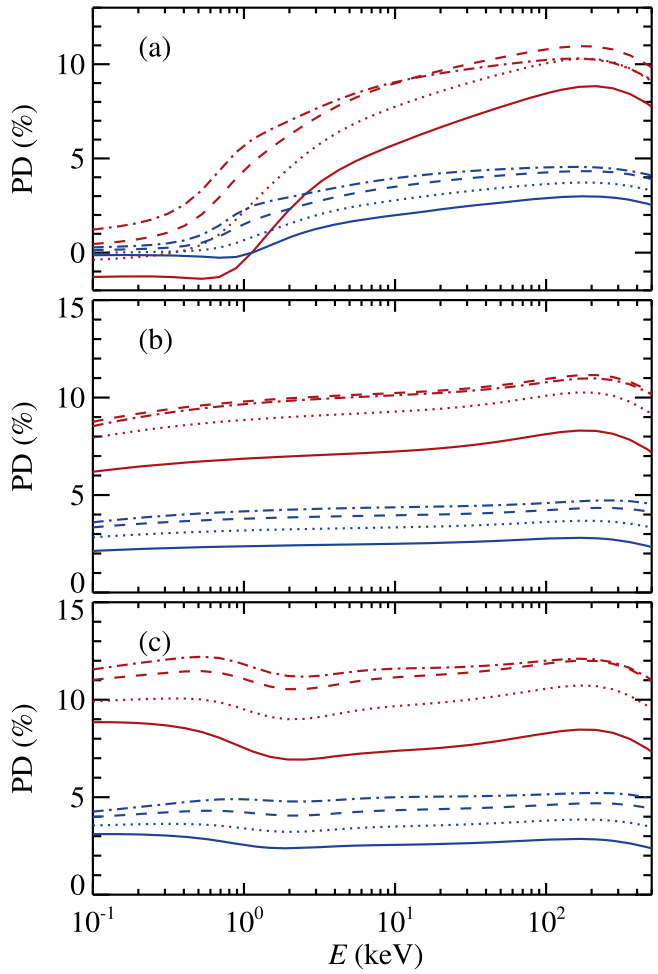

Figure 3. Energy dependence of the PD for the three models shown in Figure 2. The blue and red lines correspond to the inclinations of 30° and 60°, respectively. Solid, dotted, dashed, and dotted–dashed lines correspond to the outflow velocities of $\beta_0 = 0$, 0.2, 0.4, and 0.6, respectively. In the middle panel, the red curves for $\beta_0 = 0.4$ and 0.6 coincide.

shows that the static slab corona can produce a PD of 4% only at inclinations exceeding 60°. The outflowing corona, on the other hand, can produce this high PD at $i = 30°$ for $\beta_0 \gtrsim 0.6$.

The angular distribution of the PD for model (B) is shown in Figure 2(b). We see that the PD for the static flow of $\beta_0 = 0$ is larger than in the case of underlying disk seed photons. The reason is simple: the synchrotron seed photons take more scattering to get to the IXPE range, resulting in a more anisotropic radiation field and higher PD. The observed 4% PD is reached only at $i \approx 40°$. For $\beta_0 = 0.2$, this PD is reached at inclination of ≈33°, and the observed value of 4% at $i < 30°$ is produced when $\beta_0 \gtrsim 0.4$.

The angular distribution of the PD for model (C) is shown in Figure 2(c). It is similar to the other models but shows a slightly higher PD. We see that the PD observed in Cyg X-1 is well reproduced for the outflow velocity of $\beta_0 \approx 0.4$. We also considered a model of the seed photons from the cold clouds within the hot flow, but its results are very similar to those of models (B) and (C). We find that at all considered velocities, models (B) and (C) predict parallel polarization exceeding ∼10% at inclinations $i = 60°$–70°.

Let us now consider the energy dependence of PD. The results are shown in Figure 3 for two selected inclinations of 30° and 60°. For model (A) and the case of a static corona, polarization is negative (i.e., parallel to the disk) at photon energies where the first scattering dominates (see Appendix B for spectral decomposition in different scattering orders); it changes the sign at around 1 keV and continues to grow to higher energies where the photons undergo more than two scatterings. At $i = 30°$, the PD does not exceed 3% even at 100 keV. We note that a static slab-corona model cannot produce the hard spectra ($\Gamma \approx 1.6$) observed in Cyg X-1 once the reflection and reprocessing of radiation are taken into account: thermalization of the hard radiation in the disk would produce too many soft photons that cool the corona producing soft spectra (Poutanen et al. 2018).

Motion of the corona away from the disk can be reconciled with the spectral hardness (Beloborodov 1999) resulting also in a higher PD (see dotted, dashed, and dotted–dashed curves in Figure 3(a)). Because of the relativistic aberration, the seed photon angular distribution is less beamed along the normal in the flow-comoving frame (see Figure 4), and even single-scattered photons have polarization parallel to the disk axis (see also Beloborodov 1998). At an inclination $i < 30°$, the PD of 4% can be reached only for $\beta_0 > 0.6$, which also predicts an increasing trend of the PD with energy.

Let us now consider a truncated disk geometry with the inner hot flow. Figure 3(b) shows the results for model (B) corresponding to the synchrotron seed photons. In the static case, the PD is 2%–2.5% at $i = 30°$ (see blue solid line). Because photons reaching the IXPE range undergo many scatterings, the PD is largely energy independent (see also Figure 5). At the same inclination, the PD increases with the outflow velocity, reaching ∼4% at $\beta_0 \sim 0.4$ and 5% at $\beta_0 \sim 0.6$. At a higher inclination of $i = 60°$, the PD is about twice as large as for the $i = 30°$ case (see the set of red curves).

Finally, we consider model (C) with the hot-flow geometry and the truncated disk providing seed photons for Comptonization. The results for the case of $H/R = 1$ are shown in Figure 3(c). Here we see that the static hot flow produces nearly constant PD of ∼2.5% in the IXPE range at $i = 30°$. For the outflow velocity $\beta_0 = 0.2$, the anisotropy of the seed photons in the outflow rest frame is large enough to produce parallel polarization at a 4% level for single-scattered photons, which then drops somewhat at higher scattering orders. At $\beta_0 = 0.4$, the PD reaches 4.5%–5% and weakly depends on energy in the IXPE range. At even higher $\beta_0 = 0.6$, the PD reaches 6%.

4. Discussion and Summary

In our simulations, we ignored relativistic effects related to the rotation of the flow resulting in a rotation of the polarization plane due to relativistic effects. We note here that these effects are more important when the local emitted spectrum is blackbody-like, when relativistic aberration and Doppler boosting affect strongly the polarization vector just above the peak of the blackbody (Connors et al. 1980; Dovčiak et al. 2008; Loktev et al. 2022). However, for a power-law-like spectrum, the effect is less pronounced because of a relatively larger contribution from large radii of the flow to the observed spectrum in a given energy range. Depolarization effects are $\lesssim$1% and can explain the difference between the required inclinations for the static models found in this work and in Krawczynski et al. (2022), where relativistic effects are taken into account.

Our simulations of the dynamic corona accounting for Comptonization confirm previous results for Thomson

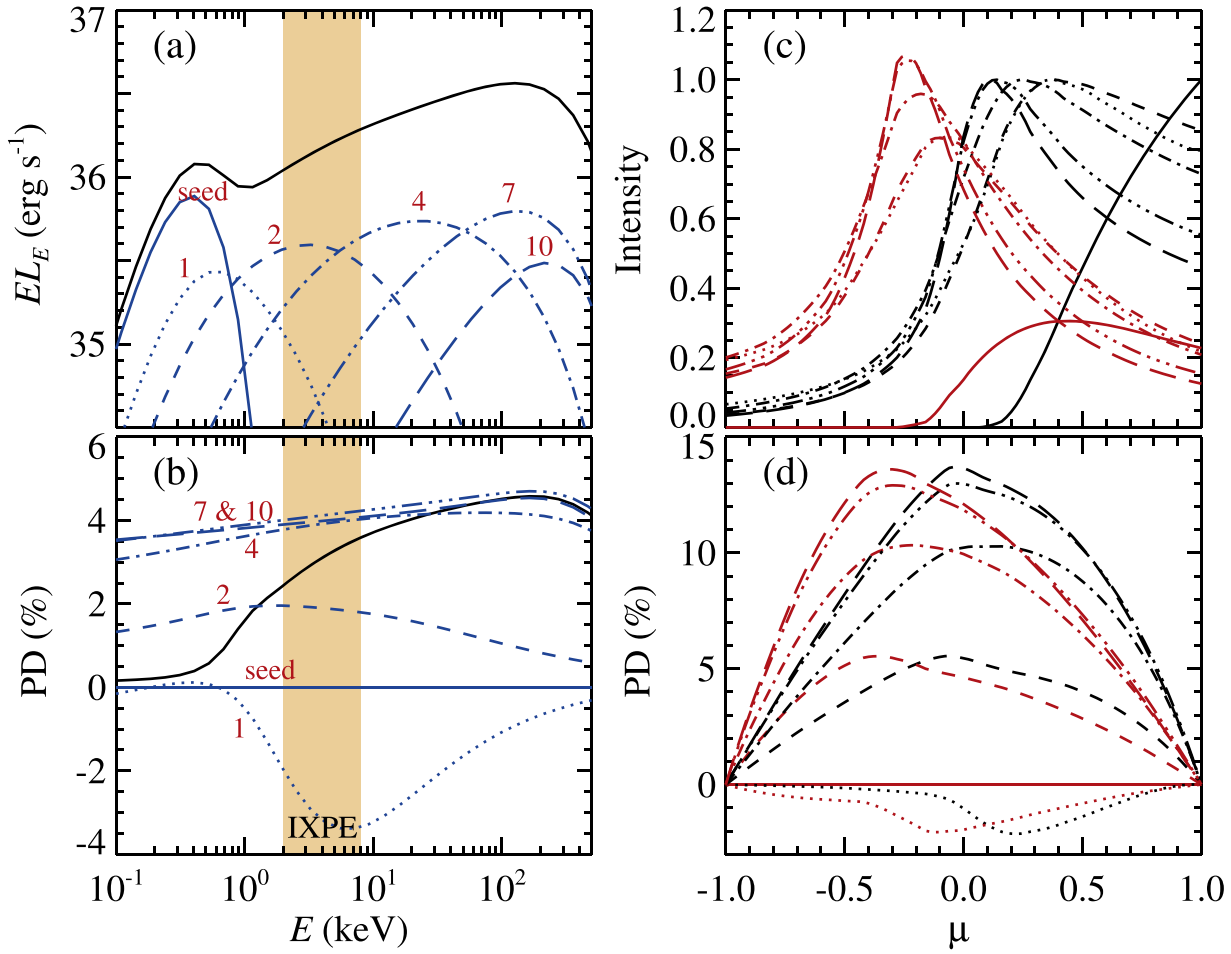

Figure 4. Spectro-polarimetric properties of model (A) of a slab corona of $T_e = 100$ keV and $T_{bb} = 0.1$ keV with the outflow of terminal velocity $\beta_0 = 0.4$. (a) Spectral energy distribution of the escaping radiation at inclination $i = 30°$ scaled to produce the angle-integrated bolometric luminosity of $L = 10^{37}$ erg s^{-1}. Blue solid, dotted, dashed, dotted–dashed, triple-dotted–dashed, and long-dashed lines show the contribution of different scattering orders $n = 0$, 1, 2, 4, 7, and 10, respectively. The black solid line gives the total spectrum. (b) The PD as a function of energy at the same inclination for the total radiation (black solid) and for different scattering orders is shown. (c) Angular distribution of the intensity at optical depth $\tau = (3/4)\tau_0$ (where $\beta = 0.3$) for the same scattering orders as above at the corresponding peaks of EI_E. The black and red curves correspond to the lab and comoving frame intensities, respectively. The lab-frame intensities are normalized to unity at the maximum. (d) Angular dependence of PD for the same scattering orders at the same energies as the intensity. The IXPE energy range is marked by a beige vertical stripe in panels (a) and (b).

scattering that the PD strongly depends on the angular distribution of incident photons (Beloborodov 1998; Beloborodov & Poutanen 1999). This effect is more important at the energies where the first scattering dominates. For the slab corona, the static model results in a rapidly growing PD in the IXPE range, but it stays below 2% for $i = 30°$. Increasing the velocity of the outflow gives a higher PD, which can reach the observed 4% at $i = 30°$ only when $\beta_0 > 0.6$. Such a high terminal velocity is required to produce the necessary photon anisotropy in the flow rest frame due to relativistic aberration. We note that the average velocity of the outflow in that case is a factor of 2 smaller and therefore is consistent with the estimate $\beta = 0.3$ by Beloborodov (1999) that is required to achieve the photon spectral slope and the reflection fraction observed in Cyg X-1. The terminal velocity is somewhat larger than the equilibrium velocity of the electron–positron pairs, which may indicate the presence of a significant amount of protons and ions in the outflow and the role of magnetic processes (rather than radiation pressure) in the flow acceleration.

The model with the internal synchrotron seed photons can reproduce an energy-independent 4% PD at $i \approx 30°$ for a more modest velocity of $\beta_0 = 0.4$–0.5 because in the IXPE range, multiple scatterings are important, and the angular distribution of seed photons does not play any role. Once we combine the mildly relativistic velocity with the anisotropy of the seed photons coming from the outer truncated disk, even higher PDs can be achieved. We conclude that in order to get 4% parallel polarization throughout the IXPE range assuming inclination of 30°, a mildly relativistic outflow velocity $\beta_0 \approx 0.4$ is needed together with either anisotropic distribution of seed soft photons coming from the outer cool disk or dominance of multiple scattering, which is a natural outcome of synchrotron photon injection at very low energies.

We also note that our model predicts PDs exceeding 10% at high inclinations $i > 60°$, which potentially could be observed in other BH X-ray binaries. Similarly high polarization is also expected from highly inclined accretion flows in Seyfert galaxies of intermediate types (see, e.g., Gianolli et al. 2023 for the case of NGC 4151).

We thank P. Abolmasov and the referee A. A. Zdziarski for valuable suggestions. J.P. and A.V. acknowledge support from the Academy of Finland grant 333112. A.M.B. is supported by NSF grant AST2009453, NASA grant 21-ATP21-0056, and

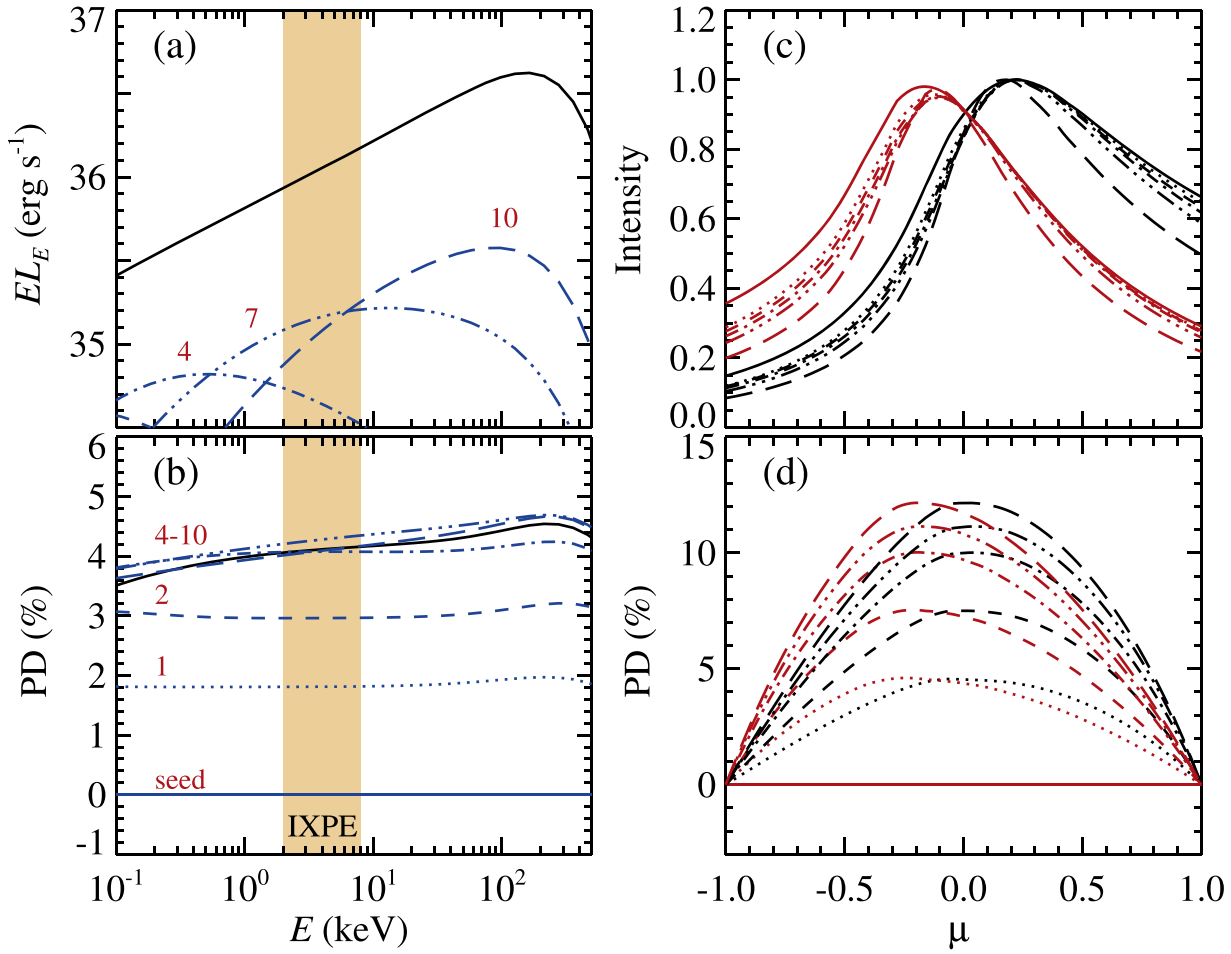

Figure 5. Same as in Figure 4 but for the seed synchrotron photons of model (B).

Simons Foundation grant 446228. Nordita is supported in part by NordForsk.

Facility: IXPE.

Software: COMPPS (Poutanen & Svensson 1996).

Appendix A
Radiative Transfer Equation

The RTE describing Comptonization of polarized radiation in the plane-parallel atmosphere in the lab frame (marked with superscript l) can be written in the form (Mihalas & Mihalas 1984; Nagirner & Poutanen 1994; Beloborodov & Poutanen 1999):

$$\mu\frac{d\boldsymbol{I}^{\rm l}(\tau,x,\mu)}{d\tau}=[1-\beta(\tau)\mu][-\sigma(x_{\rm c})\boldsymbol{I}^{\rm l}(\tau,x,\mu)+\boldsymbol{S}^{\rm l}(\tau,x,\mu)]. \quad \text{(A1)}$$

Here the photon energy is measured in units of the electron rest mass $x=E/m_{\rm e}c^2$, μ is the cosine of the angle the photon momentum makes with the slab normal, $\boldsymbol{I}=(I,\,Q)^{\rm T}$ is the Stokes vector that fully describes linear polarization (the Stokes U parameter is zero due to the azimuthal symmetry), $\boldsymbol{S}^{\rm l}$ is the source function (also Stokes vector) in the lab frame, and $\sigma(x_{\rm c})$ is the dimensionless total Compton scattering cross section (in units of the Thomson cross section $\sigma_{\rm T}$) for isotropic Maxwellian electron gas as a function of the photon energy in the comoving frame $x_{\rm c}=x/\mathcal{D}$, where $\mathcal{D}=1/[\gamma(1-\beta\mu)]$ is the Doppler factor and $\gamma=1/\sqrt{1-\beta^2}$ is the Lorentz factor of the flow. Comoving frame quantities are marked with sub- or superscript c. We define the Thomson optical depth across the slab as a measure of the column density: $d\tau=n_{\rm e}(z)\sigma_{\rm T}\,dz$, where z is the vertical coordinate and $n_{\rm e}$ is the electron concentration measured in the lab frame. The source function in the lab frame is related to that in the comoving frame by the Lorentz transformation (Rybicki & Lightman 1979):

$$\boldsymbol{S}^{\rm l}(\tau,x,\mu)=\mathcal{D}^3\,\boldsymbol{S}^{\rm c}(\tau,x_{\rm c},\mu_{\rm c}), \quad \text{(A2)}$$

where the angles are related by the aberration formulae

$$\mu_{\rm c}=\frac{\mu-\beta}{1-\beta\mu},\qquad \mu=\frac{\mu_{\rm c}+\beta}{1+\beta\mu_{\rm c}}. \quad \text{(A3)}$$

The source function in the comoving frame is

$$\boldsymbol{S}^{\rm c}(\tau,x_{\rm c},\mu_{\rm c})=x_{\rm c}^2\int_0^\infty\frac{dx'_{\rm c}}{x'^2_{\rm c}}\int_{-1}^1 d\mu'_{\rm c}\times\boldsymbol{R}(x,\mu;x'_{\rm c},\mu'_{\rm c})\boldsymbol{I}^{\rm c}(\tau,x'_{\rm c},\mu'_{\rm c})=\mathcal{R}\boldsymbol{I}^{\rm c}, \quad \text{(A4)}$$

where $\boldsymbol{R}$ is the 2×2 azimuth-averaged redistribution matrix describing Compton scattering by isotropic hot electrons (see Appendix A1 in Poutanen & Svensson 1996). The Stokes vector $\boldsymbol{I}^{\rm c}$ in the comoving frame is related to that in the lab

frame as

$$\boldsymbol{I}^{\rm c}(\tau, x_{\rm c}, \mu_{\rm c}) = \mathcal{D}^{-3}\, \boldsymbol{I}^{\rm l}(\tau, x, \mu). \tag{A5}$$

We solve the RTE using the iterative scattering method (Poutanen & Svensson 1996) accounting exactly for polarization by Compton scattering on isotropic (in the flow frame) thermal electron gas (Nagirner & Poutanen 1993). The only difference from Poutanen & Svensson (1996) is that here we account for bulk motion. At step 1, we specify the boundary condition at $\tau = 0$, either on the bottom of the slab corona or in the middle of the slab, in the case of the hot-flow–truncated disk geometry. We approximate the spectrum of seed photons (marked by index 0) by the (unpolarized) blackbody

$$\boldsymbol{I}^{\rm l}_0(\tau = 0, x, \mu) = B_x(T_{\rm bb}) \begin{pmatrix} 1 \\ 0 \end{pmatrix} \mathcal{H}(\mu_0 - |\mu|), \tag{A6}$$

where $\mathcal{H}$ is the Heaviside step function and $\mu_0 = 1$ for the slab corona, while for the truncated disk, the injection of seed photons is limited to the zenith angles corresponding to the aspect ratio of the inner hot flow $h = H/R$, $|\mu| < \mu_0 = h/\sqrt{1+h^2}$. At step 2, we use the formal solution of the RTE (Equation (A1); with zero source function $\boldsymbol{S}$) to get the intensity in all other layers of the slab:

$$\boldsymbol{I}^{\rm l}_0(\tau, x, \mu) = \boldsymbol{I}^{\rm l}_0(0, x, \mu)\, \exp(-\tau_x/\mu), \tag{A7}$$

where $\tau_x = \tau\sigma(x_{\rm c})[1 - \overline{\beta}(\tau, 0)\mu]$ is the energy- and angle-dependent optical depth measured from the bottom to a given layer and $\overline{\beta}$ is the average velocity from the slab center (or bottom for slab-corona model) $\tau = 0$ to the given τ, defined as

$$\begin{aligned} \overline{\beta}(\tau, \tau') &= \frac{1}{\tau - \tau'} \int_{\tau'}^{\tau} \beta(t)\, dt \\ &= \frac{\beta(\tau) + \beta(\tau')}{2} = \beta_0 \frac{\tau + \tau'}{2\tau_0}. \end{aligned} \tag{A8}$$

At step 3, we transform the Stokes vector $\boldsymbol{I}^{\rm l}_n$ in the lab frame for photons scattered n times to the comoving frame using Equation (A5). At step 4, we compute the source function in the comoving frame for photons scattered $n+1$ times using Equation (A4) as $\boldsymbol{S}^{\rm c}_{n+1} = \mathcal{R}\boldsymbol{I}^{\rm c}_n$. At step 5, we get the source function in the lab frame using Equation (A2). And finally at step 6, we obtain the intensity of radiation scattered $n+1$ times from the formal solution of the RTE:

$$\boldsymbol{I}^{\rm l}_{n+1}(\tau, x, \mu) = \begin{cases} \displaystyle\int_{\tau_{\rm min}}^{\tau} \frac{d\tau'}{\mu}\, \boldsymbol{S}^{\rm l}_{n+1}(\tau', x, \mu)\, [1 - \beta(\tau')\mu]\, e^{-(\tau-\tau')\sigma(x_{\rm c})[1-\overline{\beta}(\tau,\tau')\mu]/\mu}, & \mu > 0, \\ \displaystyle\int_{\tau}^{\tau_0} \frac{d\tau'}{(-\mu)}\, \boldsymbol{S}^{\rm l}_{n+1}(\tau', x, \mu)\, [1 - \beta(\tau')\mu]\, e^{-(\tau'-\tau)\sigma(x_{\rm c})[1-\overline{\beta}(\tau',\tau)\mu]/(-\mu)}, & \mu < 0, \end{cases} \tag{A9}$$

where $\tau_{\rm min} = 0$ for the slab corona and $\tau_{\rm min} = -\tau_0$ for the hot flow, and $\overline{\beta}$ is given by Equation (A8). The iteration procedure continues with steps 3–6 until the desired accuracy for the total Stokes vector $\boldsymbol{I}^{\rm l} = \sum_{n=0}^{\infty} \boldsymbol{I}^{\rm l}_n$ is achieved at all optical depths, angles, and energies.

For synchrotron seed photons, we start instead from step 4 and specify the source function in the comoving frame $\boldsymbol{S}^{\rm c}_0$. We assume it to be unpolarized, isotropic, and optical-depth independent. Its spectral energy distribution is computed assuming a thermal electron distribution of $kT_{\rm e} = 100$ keV with a weak nonthermal tail. The resulting synchrotron spectrum has a shape of a broken power law with a peak at $\sim$1 eV (Wardziński & Zdziarski 2001; Veledina et al. 2013). The iteration procedure now involves steps 5 and 6 and then 3 and 4, etc.

Appendix B
Spectro-polarimetric Properties of Outflowing Coronae

We show a few examples of simulations of polarized radiation escaping from an outflowing corona for the same three models considered in the main text. We concentrate here on the case $\beta_0 = 0.4$, which describes well Cyg X-1 data, and the observer inclination $i = 30°$. Figure 4 shows the main results for model (A), where seed unpolarized blackbody photons are injected from the bottom of outflowing corona. We see the spectral energy distribution of the total radiation as well as for selected scattering orders in panel (a). The IXPE 2–8 keV range is dominated by photons scattered two to four times in the flow. Panel (b) shows the energy dependence of the PD. The single-scattered photons have small a PD, which becomes negative in the IXPE range, because the angular distribution of the seed photons in the comoving frame of the flow is still rather beamed outwards in spite of a high velocity as is seen in panel (c). The black curves there show the angular distribution of the intensity at the optical depth $\tau = (3/4)\tau_0$ at the energy where EI_E of the corresponding scattering order peaks. The red curves are the corresponding intensities in the comoving frame. We see that relativistic aberration is responsible for anisotropy of the radiation, with the intensity of multiple scattered photons in the lab frame peaking at $\mu \approx 0.1$–0.3 ($i \approx 70°$–$80°$). On the other hand, the peak of the intensity in the comoving frame corresponds to $\mu_{\rm c} \approx -0.2$, i.e., it is directed more downwards. The angular distribution of the PD in both frames is shown in panel (d). We see that the PD grows with the scattering order. It reaches maximum roughly at the same angles where the intensity peaks. Because of the relativistic aberration, all curves in the lab frame are shifted to higher μ, so that at a given inclination, the PD grows with β.

Figure 5 shows the same quantities for model (B) with the seed synchrotron unpolarized photons, which are isotropic in the comoving frame. The PD is increasing monotonically with the number of scatterings (panel (d)), but already at around $n > 5$, very little variation is observed. Because about seven to eight scatterings are needed for seed photons to achieve the IXPE range, the PD is nearly energy independent (panel (b)). The angular distributions of both the intensity and the PD (panels (c) and (d)) saturate.

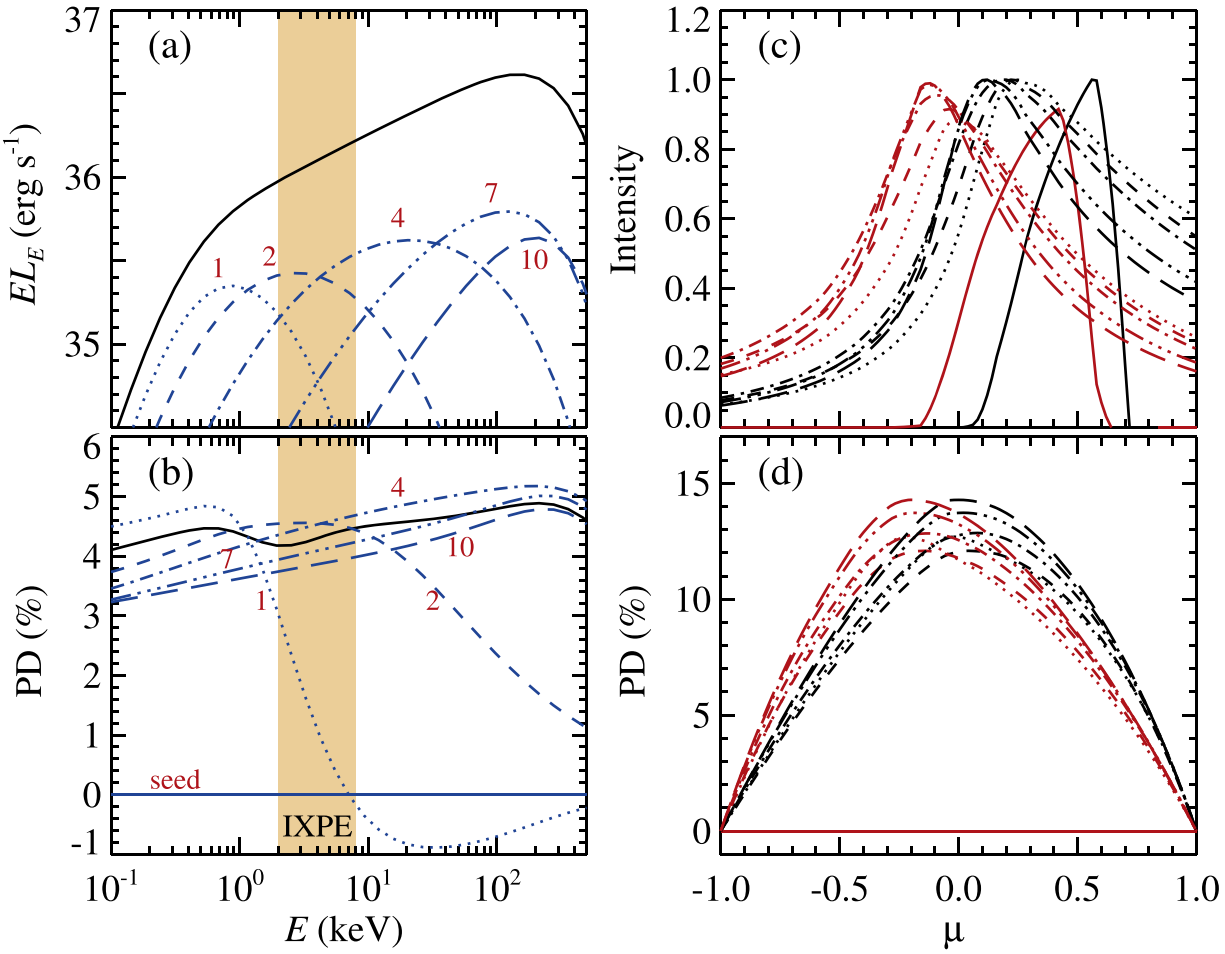

Figure 6. Same as in Figure 4 but for the seed photons from the truncated disk with the coronal aspect ratio $H/R = 1$ of model (C).

Figure 6 shows the results for model (C) with coronal aspect ratio $H/R = 1$. In this model, we see strong anisotropy of seed photons (panel (c)) both in the lab and comoving frames. This anisotropy results in a large parallel polarization reaching 12% (for the cases of high inclination) already at the first scattering. The PD increases slightly at further scatterings, having very similar behavior to the previously considered models. The IXPE range is dominated by photons scattered two to four times as in the case of model (A), but now their PD is larger. The PD is nearly energy independent as for the case of model (B), where photons scattered many more times contribute to the signal in the IXPE range.

ORCID iDs

Juri Poutanen https://orcid.org/0000-0002-0983-0049
Alexandra Veledina https://orcid.org/0000-0002-5767-7253
Andrei M. Beloborodov https://orcid.org/0000-0001-5660-3175

References

Axelsson, M., Borgonovo, L., & Larsson, S. 2005, A&A, 438, 999
Bambi, C., Brenneman, L. W., Dauser, T., et al. 2021, SSRv, 217, 65
Beloborodov, A. M. 1998, ApJL, 496, L105
Beloborodov, A. M. 1999, ApJL, 510, L123
Beloborodov, A. M., & Poutanen, J. 1999, ApJL, 517, L77
Celotti, A., Fabian, A. C., & Rees, M. J. 1992, MNRAS, 255, 419
Chandrasekhar, S. 1960, Radiative Transfer (New York: Dover)
Connors, P. A., Piran, T., & Stark, R. F. 1980, ApJ, 235, 224
Done, C., Gierliński, M., & Kubota, A. 2007, A&ARv, 15, 1
Dovčiak, M., Muleri, F., Goosmann, R. W., Karas, V., & Matt, G. 2008, MNRAS, 391, 32
Esin, A. A., Narayan, R., Cui, W., Grove, J. E., & Zhang, S.-N. 1998, ApJ, 505, 854
Fender, R. P. 2001, MNRAS, 322, 31
Gianolli, V. E., Kim, D. E., Bianchi, S., et al. 2023, arXiv:2303.12541
Gierlinski, M., Zdziarski, A. A., Done, C., et al. 1997, MNRAS, 288, 958
Gierliński, M., Zdziarski, A. A., Poutanen, J., et al. 1999, MNRAS, 309, 496
Haardt, F., & Maraschi, L. 1993, ApJ, 413, 507
Ibragimov, A., Poutanen, J., Gilfanov, M., Zdziarski, A. A., & Shrader, C. R. 2005, MNRAS, 362, 1435
Ichimaru, S. 1977, ApJ, 214, 840
Krawczynski, H., Muleri, F., Dovčiak, M., et al. 2022, Sci, 378, 650
Lightman, A. P., & Shapiro, S. L. 1976, ApJ, 203, 701
Liska, M. T. P., Musoke, G., Tchekhovskoy, A., Porth, O., & Beloborodov, A. M. 2022, ApJL, 935, L1
Loktev, V., Veledina, A., & Poutanen, J. 2022, A&A, 660, A25
Malzac, J., & Belmont, R. 2009, MNRAS, 392, 570
Malzac, J., Beloborodov, A. M., & Poutanen, J. 2001, MNRAS, 326, 417
Malzac, J., Dumont, A. M., & Mouchet, M. 2005, A&A, 430, 761
McConnell, M. L., Zdziarski, A. A., Bennett, K., et al. 2002, ApJ, 572, 984
Mihalas, D., & Mihalas, B. W. 1984, Foundations of Radiation Hydrodynamics (Mineola, NY: Dover)
Miller-Jones, J. C. A., Bahramian, A., Orosz, J. A., et al. 2021, Sci, 371, 1046
Nagirner, D. I., & Poutanen, J. 1993, A&A, 275, 325
Nagirner, D. I., & Poutanen, J. 1994, ASPRv., 9, 1
Nayakshin, S., & Dove, J. B. 2001, ApJ, 560, 885
Novikov, D. I., & Thorne, K. S. 1973, in Les Astres Occlus, ed. B. Witt & C. Witt (New York: Gordon and Breach), 343
Pottschmidt, K., Wilms, J., Nowak, M. A., et al. 2003, A&A, 407, 1039
Poutanen, J., & Coppi, P. S. 1998, PhST, T77, 57
Poutanen, J., Krolik, J. H., & Ryde, F. 1997, MNRAS, 292, L21
Poutanen, J., & Svensson, R. 1996, ApJ, 470, 249
Poutanen, J., & Veledina, A. 2014, SSRv, 183, 61
Poutanen, J., Veledina, A., Berdyugin, A. V., et al. 2022, Sci, 375, 874

Poutanen, J., Veledina, A., & Zdziarski, A. A. 2018, A&A, 614, A79
Poutanen, J., & Vurm, I. 2009, ApJL, 690, L97
Remillard, R. A., & McClintock, J. E. 2006, ARA&A, 44, 49
Rybicki, G. B., & Lightman, A. P. 1979, Radiative Processes in Astrophysics (New York: Wiley)
Schnittman, J. D., & Krolik, J. H. 2010, ApJ, 712, 908
Shakura, N. I., & Sunyaev, R. A. 1973, A&A, 500, 33
Shapiro, S. L., Lightman, A. P., & Eardley, D. M. 1976, ApJ, 204, 187
Stern, B. E., Poutanen, J., Svensson, R., Sikora, M., & Begelman, M. C. 1995, ApJL, 449, L13
Stirling, A. M., Spencer, R. E., de la Force, C. J., et al. 2001, MNRAS, 327, 1273
Sunyaev, R. A., & Titarchuk, L. G. 1985, A&A, 143, 374
Svensson, R. 1984, MNRAS, 209, 175
Veledina, A., Poutanen, J., & Vurm, I. 2013, MNRAS, 430, 3196
Wardziński, G., & Zdziarski, A. A. 2001, MNRAS, 325, 963
Weisskopf, M. C., Soffitta, P., Baldini, L., et al. 2022, JATIS, 8, 026002
Yuan, F., & Narayan, R. 2014, ARA&A, 52, 529
Zdziarski, A. A., & Gierliński, M. 2004, PThPS, 155, 99
Zdziarski, A. A., Grove, J. E., Poutanen, J., Rao, A. R., & Vadawale, S. V. 2001, ApJL, 554, L45
Zdziarski, A. A., Lubiński, P., Gilfanov, M., & Revnivtsev, M. 2003, MNRAS, 342, 355
Zdziarski, A. A., Lubiński, P., & Smith, D. A. 1999, MNRAS, 303, L11